Nano Research
https://doi.org/10.1007/s12274-017-1925-4
Research Article
ISSN 1998-0124
CN 11-5974/O4

Acidity-triggered TAT-presenting nanocarriers augment tumor retention and nuclear translocation of drugs

Wei Jiang[1], Jilong Wang[2], Jinbin Yang[3], Zhiwei He[4], Zhenhui Hou[4], Yingli Luo[2], Li Wang[2], Jing Liu[2], Houbing Zhang[1], Yangyang Zhao[2], Guoqing Zhang[1], Fang Huang[4], Xuechang Zhou[3], Lifeng Yan[1] (✉), Xianzhu Yang[5] (✉), Yucai Wang[2] (✉), and Jun Wang[5]

[1] *Hefei National Laboratory for Physical Sciences at the Microscale, University of Science and Technology of China, Hefei 230027, China*
[2] *The CAS Key Laboratory of Innate Immunity and Chronic Disease, School of Life Sciences and Medical Center, University of Science and Technology of China, Hefei 230027, China*
[3] *School of Chemistry and Environmental Engineering, Shenzhen University, Shenzhen 518060, China*
[4] *School of Earth and Space Sciences, University of Science and Technology of China, Hefei 230027, China*
[5] *Institutes for Life Sciences, School of Medicine and National Engineering Research Center for Tissue Restoration and Reconstruction, South China University of Technology, Guangzhou 510006, China*

Received: 1 October 2017
Revised: 13 November 2017
Accepted: 16 November 2017

KEYWORDS
acidic tumor microenvironment,
cancer therapy,
cellular nucleus translocation,
ligand presenting nanomedicines,
tumor retention

ABSTRACT

Hierarchical targeting strategy can combat the sequential drug delivery barriers by changing their properties with response to tumor stimuli. Among these strategies, much less attention has been paid to address the issues of rapid tumor clearance and insufficient cellular translocation. In this work, we demonstrate that a transactivator of transcription (TAT)-presenting nanomedicine (^{DA}TAT-NP/Pt), apart from improving tumor accumulation and cellular uptake, can simultaneously enhance tumor retention and promote nuclear translocation of encapsulated platinum prodrugs, and thus improve therapeutic efficacy. Specifically, a protecting 2,3-dimethylmaleic anhydride (DA) corona on the nanomedicine prevented the TAT peptide from serum. ^{DA}TAT-NP/Pt efficiently accumulated at the tumor site through the enhanced permeability and retention (EPR) effect, followed by acid-triggered TAT presenting within the tumor acidic microenvironment (pH ~ 6.8). The exposed TAT peptide augmented tumor retention and nuclear translocation of ^{DA}TAT-NP/Pt. We used a tumor-on-a-chip microfluidic system to real-time mimic and analyze tumor accumulation and retention at physiological flow conditions and revealed that surface absorption of nanomedicines on tumors was critical in determining their tumor retention and clearance. Furthermore, the TAT peptide rapidly translocated the ^{DA}TAT-NP/Pt into the perinuclear region, allowing for higher nuclear platinum concentrations and increased Pt-DNA adduct formation in nuclei, which consequently reversed cisplatin resistance. Our work presents a new strategy to overcome path-ophysiological barriers of tumor clearance and insufficient cellular translocation and provides new insights for the design of cancer nanomedicines.

Address correspondence to Yucai Wang, yucaiwang@ustc.edu.cn; Xianzhu Yang, yangxz@hfut.edu.cn; Lifeng Yan, lfyan@ustc.edu.cn

1 Introduction

Nanomedicines (NMs) hold promise in cancer chemotherapy by which they can improve the therapeutic efficacy while suppressing the adverse effects of anticancer drugs [1, 2]. The improved efficacy was typically associated with preferential tumor accumulation owing to the enhanced permeability and retention (EPR) effect, also known as passive targeting. The EPR effect exposits the leaky tumor vasculature endothelium and poor functional lymphatic drainage and allows NMs to efficiently retain in the tumor rather than other normal tissues. Actively targeting NMs by surface modification with targeting ligands, can further improve cellular uptake and the subsequent therapeutic effect by selectively targeting cells overexpressing specific receptors [3]. Unfortunately, ligands presented at the surface of NMs may have undesirable interactions with serum proteins, which results in accelerated reticuloendothelial system (RES) clearance and unfavorable pharmacokinetics and biodistribution [4, 5]. To address the paradox, hierarchical targeting NMs, which can change their properties by responding to either internal and intrinsic environments of tumor (such as acidic pH, temperature, redox condition, ATP, or the activity of a certain enzyme) or external and artificial stimuli (such as a magnetic field, ultrasound, and photo-irradiation), have been extensively developed [6–13]. The hierarchical targeting strategy, generally consisting of at least two targeting stages, simultaneously possesses high tumor accumulation based on the EPR effect and efficient cellular internalization based on selectively binding with tumor cell membranes.

Among the tremendous efforts made in the design of hierarchical targeting NMs, much less is known about other barriers encountered during drug transition processes such as rapid tumor clearance and insufficient nuclear translocation [14]. Recent studies have shown that NMs could re-enter the blood or lymphatic vessels from tumors and resulted in less effective therapeutic effect [15, 16]. The tumor retention and treatment outcome of NMs can be improved by *in situ* self-assembly or crosslinking of small-molecules under pathological environments to form fibrous nanostructures, which results in the so-called aggregation induced retention (AIR) effect [17]. More recently, Chan et. al., have studied the underlying mechanisms of tumor clearance and revealed that modification by covalent conjugation with polyethylene glycol (PEG) (PEGylation) of NMs inhibits cell and extracellular matrix (ECM) binding at the interface between tumors and bodily fluids. NMs not immobilized by the ECM can be rapidly excluded from tumors by interstitial flow [18]. Therefore, enhancing the interaction of NMs with the ECM and increasing tumor retention, is critical for realizing their therapeutic effects.

Insufficient cellular translocation to the nuclei of target tumor cells limits NM efficiency and remains another barrier in the success of these medicines [19]. In fact, many types of anticancer drugs are known to work in the nucleus. The released drugs from NMs into the cytoplasm would be exposed to efflux transporters, which hinder the translocation of drug molecules to the nucleus [20]. In addition, detoxification-related molecules in the cytoplasm, such as glutathione (GSH) and other GSH-related enzymes, can induce unwanted reactions and decrease cellular sensitivity to drugs [21]. For instance, an elevated level of GSH in cancer cells can react with cisplatin, preventing the formation of platinum-DNA adducts in nuclei and thus causing drug resistance [22]. Therefore, a more elegant delivery carrier design should also take nuclear uptake into consideration to optimize the overall efficacy of therapeutic nanoparticles. Nucleus-targeting drug delivery, in which drugs are directly delivered into nuclei, has been shown to induce more pronounced cytotoxicity against cancer cells [23–26]. This strategy however is limited by the size of the nuclear pore (pore size about 10–50 nm) [27–29].

In this work, we demonstrate that a hierarchical targeting strategy based on transactivator of transcription (TAT)-presentation can, apart from improving tumor accumulation and cellular uptake, simultaneously enhance tumor retention and promote nuclear translocation of encapsulated drugs. This design was based on the following rationales. First, the TAT peptide derived from the protein transduction domain of the human immunodeficiency virus (HIV) has proved capable of promoting cellular internalization and actively transporting cargo into cellular nuclei.

This is accomplished via binding to the import receptors, importin α and β (karyopherin), or heterologous β-galactosidase protein, which subsequently target the cargo to the nuclear pore complexes (NPCs) and thereby facilitate entry into cell nuclei [30–33]. Second, the cationic nature of the TAT peptide can facilitate binding to ECM protein fibers as well as the cells at the interface between tumor and bodily fluids, which is expected to reduce tumor clearance [18]. Third, given that the positively charged TAT peptide also results in recognition by the RES and consequently causes rapid removal from blood circulation, we further modified the TAT peptide with a tumor acidity-activated mask [34]. As shown in Fig. 1, the TAT peptide of the ^{DA}TAT-NP is masked by 2,3-dimethylmaleic anhydride (DA) and could be reactivated by an acidity increase in the tumor microenvironment. Therefore, the ^{DA}TAT-NP is able to prolong circulation in the blood and accumulate at tumor tissues upon masking of the TAT peptide. Subsequently, the extracellular pH (pH_e) of tumor tissue (ca. pH 6.3–7.0), which is slightly lower than that of normal tissue and blood (ca. pH 7.2–7.4) [35, 36], is capable of reactivating the masked TAT peptide to markedly enhance binding of TAT with the ECM and tumor cells and facilitating cellular translocation to the perinuclear region. The cisplatin prodrug was used as a model drug because it is among the most potent clinical anticancer chemotherapeutics against a wide variety of tumors, and acts by disrupting the DNA structural set-up in cancer cell nuclei [37, 38]. ^{DA}TAT-NP/Pt can be translocated rapidly to the perinuclear region, where it releases the encapsulated platinum prodrug Pt(IV) complexes.

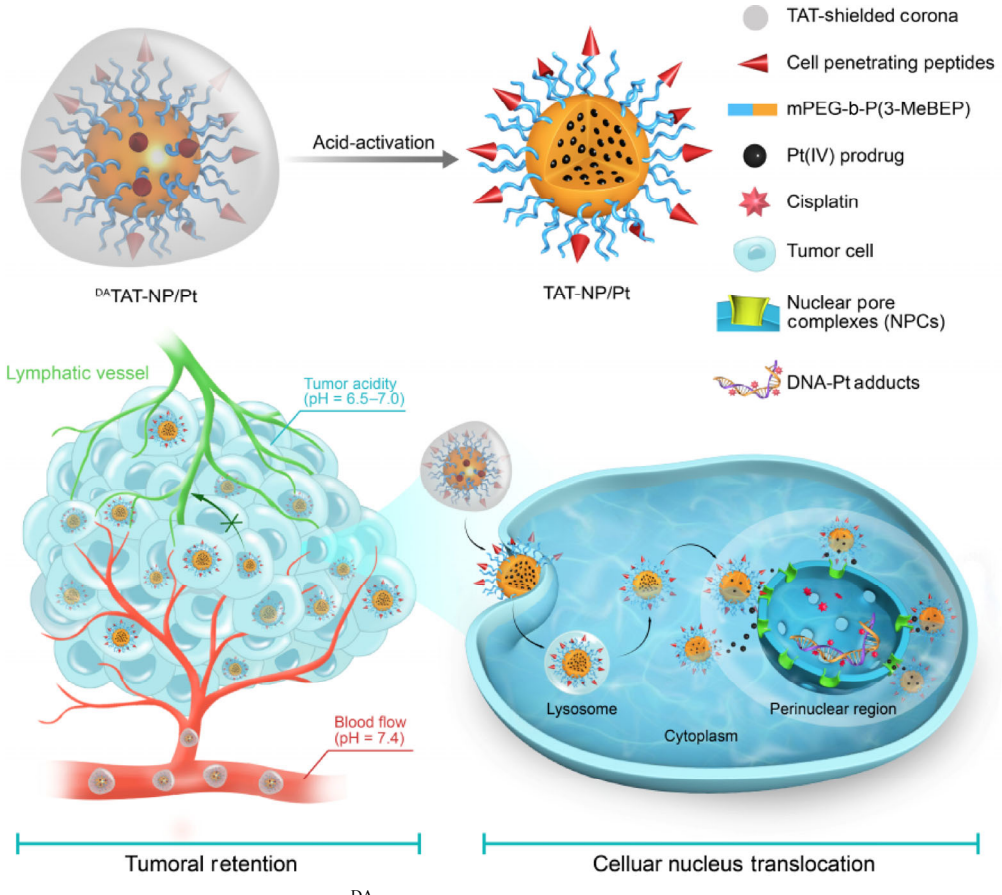

Figure 1 Schematic illustration of the structure of ^{DA}TAT-NP/Pt and its pH_e-activatable characteristics. With the protective DA corona, ^{DA}TAT-NP/Pt efficiently accumulates at the tumor site through the enhanced permeability and retention effect, followed by acidity-triggered TAT presentation within the tumor acidic microenvironment (pH ~ 6.8). The interaction of the exposed TAT with the extracellular matrix and cells prevents tumor clearance from blood and lymphatic vessels. Thereafter, TAT peptide facilitates nuclear translocation of ^{DA}TAT-NP/Pt and increases DNA-Pt adduct formation.

These prodrugs are in turn reduced to generate the cytotoxic platinum(II) species, resulting in the formation of Pt-DNA adducts in cell nuclei [39, 40]. In this work, the *in vivo* fate of ^{DA}TAT-NP during the above four successive processes and the overall antitumor efficacy in cisplatin-resistant tumor xenografts have been comprehensively evaluated.

2 Experimental

2.1 Materials and characterization

Cisplatin was purchased from Shandong Boyuan Pharmaceutical Co., Ltd. (Shandong, China). 3-(4,5-Dimethylthiazol-2-yl)-2,5-diphenyltetra-zolium bromide (MTT) was purchased from Sangon Biotech (Shanghai, China). The Annexin-V-Fluos Staining Kit was purchased from Roche Diagnostics (Indianapolis, IN, USA). Ultra-purified water was prepared using a Milli-Q System (Millipore, Bedford, MA, USA). Alexa Fluor® 488 phalloidin and 4,6-diamidino-2-phenylindol (DAPI) were purchased from Sigma-Aldrich (St. Louis, MO, USA). Hydrophobic fluorescent dye Cy5.5 and rhodamine B (RhoB)-poly(ε-caprolactone) (PCL) were synthesized by a method described previously [41].

Polymers were characterized by NMR Bruker AVANCE III 400 MHz spectrometer (Bruker Scientific Corporation Ltd., Switzerland) in deuterated reagent ($CDCl_3$ or DMSO-d_6). Molecular weights of the samples were determined by Gel Permeation Chromatography (GPC, Waters, Milford, MA, USA) as described previously [42]. The size and zeta potential measurements were carried out in aqueous solution using a Malvern ZS90 dynamic light scattering (DLS) instrument (Malvern Instruments Ltd., England) with a He-Ne laser (633 nm) and 90 collecting optics. The data were analyzed using a Malvern Dispersion Technology Software 5.10. Morphology of NMs was examined by Tecnai Cryo-TEM (FEI, Hillsboro, OR, USA) at an accelerating voltage of 200 kV. The amount of platinum was determined by inductively coupled plasma mass spectrometer (ICP-MS) (ELAN DRC II with Axial Field Technology, PerkinElmer, Waltham, MA, USA).

2.2 Degradation of DA in ^{DA}TAT-NP/Pt

Degradation of DA in ^{DA}TAT-NP/Pt was monitored using fluorescamine (98%, Shanghai Macklin Biochemical Co. Ltd., Shanghai, China) as the sensor. ^{DA}TAT-NP/Pt was dispersed in phosphate buffer (PB, 0.02 M) at pH 6.8 and 7.4 for preset times at 37 ˚C. Subsequently, fluorescamine solution in N,N-dimethylformamide (DMF) (2 mg·mL^{-1}, 0.2 mL) was added to samples (5 mg·mL^{-1}, 1.0 mL). After further incubation for 10 min at 37 ˚C, the fluorescence intensity (Fs) was tested via a RF-5301PC spectrophotometer (Shimadzu, Kyoto, Japan) (excitation: 390 nm, emission: 483 nm). Fo was defined as the fluorescence intensity of TAT-NP/Pt with the same concentration, which contained the primary amine group equivalent to amide bonds of ^{DA}TAT-NP/Pt was hydrolyzed, while Fc was defined as the fluorescence of phosphate-buffered saline (PBS) control. The degradation rate of DA was calculated as following

$$\text{Degradation rate of DA} = (Fs-Fc)/(Fo-Fc) \times 100\% \quad (1)$$

The degradations of SA in ^{SA}TAT-NP/Pt at pH 7.4 or 6.8 were also investigated with the same method.

2.3 Zeta potential changes in different pH conditions

TAT-NP/Pt, ^{SA}TAT-NP/Pt, or ^{DA}TAT-NP/Pt were incubated in PB (0.02 M) at pH 7.4 or 6.8 at 37 ˚C. At designated time intervals, an aliquot of the NMs solution was withdrawn, and the zeta potential was measured by DLS.

2.4 Cellular uptake study

The cellular uptake of ^{DA}TAT-NP/Pt and the control ^{SA}TAT-NP/Pt, and TAT-NP/Pt were observed via flow cytometry (BD Biosciences, Bedford, MA, USA) and confocal laser scanning microscopy (CLSM) (LSM 710, Carl Zeiss Inc., Germany). For flow cytometry, A549R cells were seeded in 24-well cell culture plates at a density of 8 × 10^4 cells per well. After culturing overnight, culture media was replaced with fresh media containing RhoB-labeled TAT-NP/Pt, ^{SA}TAT-NP/Pt, and ^{DA}TAT-NP/Pt at pH 7.4 or 6.8 for 4 h. The cells were then washed three times with PBS, trypsinized, and collected for fluorescence activated cell sorting (FACS) analyses.

For CLSM observation, A549R cells were seeded on coverslips in a 24-well plate at a density of 4 × 10^4

cells per well. After culturing overnight, the cells were treated with the NMs as mentioned above. After incubation for 4 h, the cells were washed three times with PBS, and then the cytoskeleton and cell nuclei were stained by Alexa Fluor 488 (green) and DAPI (blue), respectively, according to the manufacturer's instructions. Coverslips were mounted on glass microscope slides with a drop of anti-fade mounting media (Sigma-Aldrich, St. Louis, MO, USA) to reduce fluorescence photobleaching, and then visualized by CLSM.

In addition, A549R cells were seeded in 24-well cell culture plates at a density of 8×10^4 cells per well and cultured overnight. The cells were treated with PBS, free cisplatin, TAT-NP/Pt, ^{SA}TAT-NP/Pt, and ^{DA}TAT-NP/Pt at pH 7.4 and 6.8 for 2, 4, 8, and 12 h, respectively, at an equivalent platinum concentration of 50 μM. After incubation, the cells were washed with cold PBS, collected, and analyzed by ICP-MS.

2.5 Localization of NMs in A549R cells

The A549R cells were seeded on coverslips in a 24-well plate at a density of 4×10^4 cells per well and cultured overnight. After incubation with the above mentioned RhoB-labeled NMs at pH 6.8 for 10 h, the cells were washed with cold PBS. The cell nuclei were stained with DAPI (blue). The localization of NMs was visualized under CLSM.

2.6 Cellular DNA-Pt adduct detection

A549R cells were seeded in cell culture round dishes (Sigma Aldrich, 10 cm × 10 cm) at a density of 6×10^6 cells per dish and cultured overnight. The cells were then incubated with free cisplatin, TAT-NP/Pt, ^{SA}TAT-NP/Pt, and ^{DA}TAT-NP/Pt at an equivalent platinum concentration of 50 μM. After incubation at pH 7.4 and 6.8 for 2, 4, 8, and 12 h, respectively, the cells were washed with PBS and harvested. The intracellular genomic DNA was extracted using Genomic DNA Mini Preparation Kit (Beyotime, Shanghai, China), and the DNA concentration was determined by NanoDrop 2000 Spectrophotometer (Thermo Fisher Scientific, Wilmington, DE, USA). The DNA-Pt adducts were digested with aqua regia, and the amount of platinum was analyzed by ICP-MS.

2.7 Animals and tumor model

Male nonobese diabetic/severe combined immunodeficiency (NOD/SCID) mice (~ 6–8 weeks old) were purchased from Beijing HFK Bioscience (Beijing, China). All animals received care in compliance with the guidelines outlined in the Guide for the Care and Use of Laboratory Animals, and all procedures were approved by the University of Science and Technology of China Animal Care and Use Committee. The xenograft tumor model was generated by injection of 5×10^6 A549R cells (100 μL) with 10% Matrigel (BD Bioscience, Franklin Lakes, NJ, USA) into the right flank of NOD/SCID mice.

2.8 Pharmacokinetic studies *in vivo*

Free cisplatin, TAT-NP/Pt, ^{SA}TAT-NP/Pt, and ^{DA}TAT-NP/Pt were injected into the tail vein of male NOD/SCID mice at an equivalent dose of 2.0 mg platinum per kg mouse weight (n = 4 for each group). Blood samples were collected from the retro-orbital plexus of eyes at different time intervals. The plasma was obtained by centrifuging the blood at 5,000 rpm for 10 min at 4 ˚C. The resulting supernatant (50 μL) was subsequently digested with aqua regia before the platinum content was analyzed using ICP-MS.

2.9 *In vivo* NMs distribution and *ex vivo* tumor accumulation

NOD/SCID male mice bearing A549R xenografts were intravenously injected with Cy5.5-labeled TAT-NP/Pt, ^{SA}TAT-NP/Pt, and ^{DA}TAT-NP/Pt. The dose of Cy5.5 was 0.5 mg per kg mouse body weight. At the preset times, *in vivo* fluorescent images were acquired on the Xenogen IVIS Lumina system (Caliper Life Sciences, Alameda, CA, USA). Moreover, after 24, 48, and 72 h, the organs of mice including heart, lung, liver, spleen, kidney, brain, and tumor were collected. Fluorescent images were acquired on the Xenogen IVIS Lumina system as well.

2.10 Microfluidic imitated accumulation and retention of ^{DA}TAT-NP/Pt in tumor-like spheroids of A549R cells

RhoB-labeled TAT-NP/Pt, ^{SA}TAT-NP/Pt, and ^{DA}TAT-

NP/Pt were pre-incubated in pH 6.8 imaging media for 4 h before injected into a microfluidic channel. The microfluidic device was fixed on a microscope stage. Flow rate was controlled using a syringe pump. NM accumulation images were obtained using a 20× objective at a 546-nm excitation wavelength on a confocal microscope (Olympus IX-83, Tokyo, Japan). Images were taken at 15 min intervals for 1 h at a flow rate of 450 μL·h^{-1}. Before taking images, fresh media without NMs was fluxed for 5 min at a flow rate of 50 μL·min^{-1}. This was done in order to remove NMs adhered to the surface of spheroids. The spheroids were then flushed with fresh media for another 1 h at a flow rate of 450 μL·h^{-1}. Fluorescence distribution was analyzed in ImageJ by drawing a freehand contour around the spheroid. For every time point, we selected four images at different *z*-axis planes between 20 and 80 μm to determine the accumulation of NMs (Fig. S10 in the Electronic Supplementary Material (ESM)). The intensity of accumulation was obtained by taking the mean fluorescence and normalizing to fluorescence of the surrounding media. All experiments were performed on three spheroids.

2.11 Tumor suppression study

When the tumor volumes were around 100 mm^3 on the 14th day, the mice were randomly divided into six groups (five mice per group) and given intravenous injections of cisplatin, TAT-NP/Pt, ^{SA}TAT-NP/Pt, and ^{DA}TAT-NP/Pt at an equivalent platinum dose of 2.0 mg per kg mouse weight. There was also a control PBS group and a blank nanoparticle ^{DA}TAT-NP group. The injections were given on the 14th, 20th, and 26th day post-injection with A549R cells. Tumor growths were monitored by measuring the perpendicular diameter of the tumor using calipers every two days. The estimated volume was calculated according to the formula

$$\text{Tumor volume (mm}^3\text{)} = 0.5 \times \text{length} \times \text{width}^2 \quad (2)$$

The weight of each mouse was also measured every two days.

2.12 Statistical analysis

The statistical significance was assessed using the Student's *t*-test (two-tailed); $^*p < 0.05$ was considered statistically significant in all analysis (95% confidence level).

3 Results and discussion

3.1 Preparation and characterization of Pt(IV) prodrug-encapsulated NMs modified with a pH$_e$-activatable TAT peptide

To prepare the pH$_e$-activatable ^{DA}TAT-NP/Pt, we first synthesized an amphiphilic diblock polymer of poly(ethylene glycol) and poly(2-(3-methyl-1-butoxy)-2-oxo-1,3,2-dioxaphospholane) bearing a maleimide end group by the ring-opening polymerization of the cyclic monomer 2-(3-methyl-1-butoxy)-2-oxo-1,3,2-dioxaphospholane (i.e., 3-methylbutyl ethylene phosphate, 3-MeBEP) using linear heterobifunctional polyethylene glycol with a maleimide and a hydroxyl group (Mal-PEG$_{113}$-OH, M_n = 5,000 g·mol^{-1}) as an initiator (Scheme S1 in the ESM). The polymer is denoted as Mal-PEG$_{113}$-b-P(3-MeBEP)$_{50}$, where the subscript number represents the degrees of polymerization according to ^{1}H NMR analysis. The successful synthesis of the polymer was verified by GPC, as the obtained Mal-PEG$_{113}$-b-P(3-MeBEP)$_{50}$ exhibited a shorter retention time while maintaining a unimodal peak compared with the Mal-PEG$_{113}$-OH macroinitiator (Fig. S1 in the ESM). Subsequently, the TAT peptide "YGRKKRRQRRRC" [43] was tethered to the maleimide end group to obtain the TAT peptide-functionalized polymer TAT-PEG$_{113}$-b-P(3-MeBEP)$_{50}$. After conjugation, the double bond of the maleimide (6.7 ppm, peak a, Fig. S2 in the ESM) diminished in the ^{1}H NMR spectrum. Based on the result of Ellman's assay, 78.3% of the maleimide end group was successfully conjugated with the TAT peptide. Finally, the amines of the lysine residues of the TAT peptide were further modified with DA to obtain the polymer ^{DA}TAT-PEG$_{113}$-b-P(3-MeBEP)$_{50}$. As a non-pH$_e$-responsive TAT peptide masking control, the lysine amines were modified with succinic anhydride (SA). The DA and SA conjugation efficiency with TAT-PEG$_{113}$-b-P(3-MeBEP)$_{50}$ were calculated to be approximately 92.0% and 93.8%, respectively, using ^{1}H NMR spectrum analyses (Figs. S3 and S4 in the

ESM). Furthermore, amphiphilic diblock polymer $mPEG_{113}$-b-P(3-MeBEP)$_{51}$ with a methoxy terminal group instead of the TAT peptide was successfully synthesized by replacing Mal-PEG_{113}-OH with $mPEG_{113}$-OH (Fig. S5 in the ESM). The obtained ^{DA}TAT-PEG_{113}-b-P(3-MeBEP)$_{50}$, $mPEG_{113}$-b-P(3-MeBEP)$_{51}$, and hydrophobic Pt(IV) prodrug c,c,t-[$Pt(NH_3)_2Cl_2(O_2C(CH_2)_8CH_3)_2$] [44] were used to prepare the tumor acidity-responsive Pt(IV)-prodrug-encapsulated ^{DA}TAT-NP/Pt through the dialysis method, and the two non-pH_e responsive controls ^{SA}TAT-NP/Pt and TAT-NP/Pt were prepared similarly by replacing ^{DA}TAT-PEG_{113}-b-P(3-MeBEP)$_{50}$ with ^{SA}TAT-PEG_{113}-b-P(3-MeBEP)$_{50}$ and TAT-PEG_{113}-b-P(3-MeBEP)$_{50}$, respectively. For all the three NMs, the loading content of platinum was ca. 3.0%.

According to our design, the amide bond formed between the TAT peptide lysine residual amines and DA is stable under physiological pH conditions (i.e., pH 7.4), but rapidly degrades to recover the TAT peptide in the slightly more acidic tumor environment (i.e., pH 6.8) [45]. To test our hypothesis, we incubated ^{DA}TAT-NP/Pt and ^{SA}TAT-NP/Pt in pH 7.4 and 6.8 phosphate buffers (0.02 M), and then quantified the recovered amines via the degradation of amide bonds using fluorescamine as a sensor in real time (Fig. 2(a)). Fluorescamine is fluorogenic upon reacting with primary amines [23]. For the ^{DA}TAT-NP/Pt, 95% of the amides were hydrolyzed and converted to amine bonds within 2 h at pH 6.8, while only 38% of the amide bonds were degraded at pH 7.4 during the same period at 37 °C. In contrast, for ^{SA}TAT-NP/Pt, approximately 12% of the amide bonds were hydrolyzed under the same conditions and an invariant degradation rate was observed at either pH 7.4 or 6.8. Moreover, the zeta potential changes of ^{DA}TAT-NP/Pt and ^{SA}TAT-NP/Pt were monitored. As shown in Fig. 2(b), incubation of ^{DA}TAT-NP/Pt at pH 6.8 led to a quick increase in the zeta potential from −20.2 to −3.6 mV, reaching a value similar to that of the TAT-NP/Pt, which displayed a complete recovery of amines after acid treatment as observed above (Fig. 2(a)). In contrast, the zeta potential

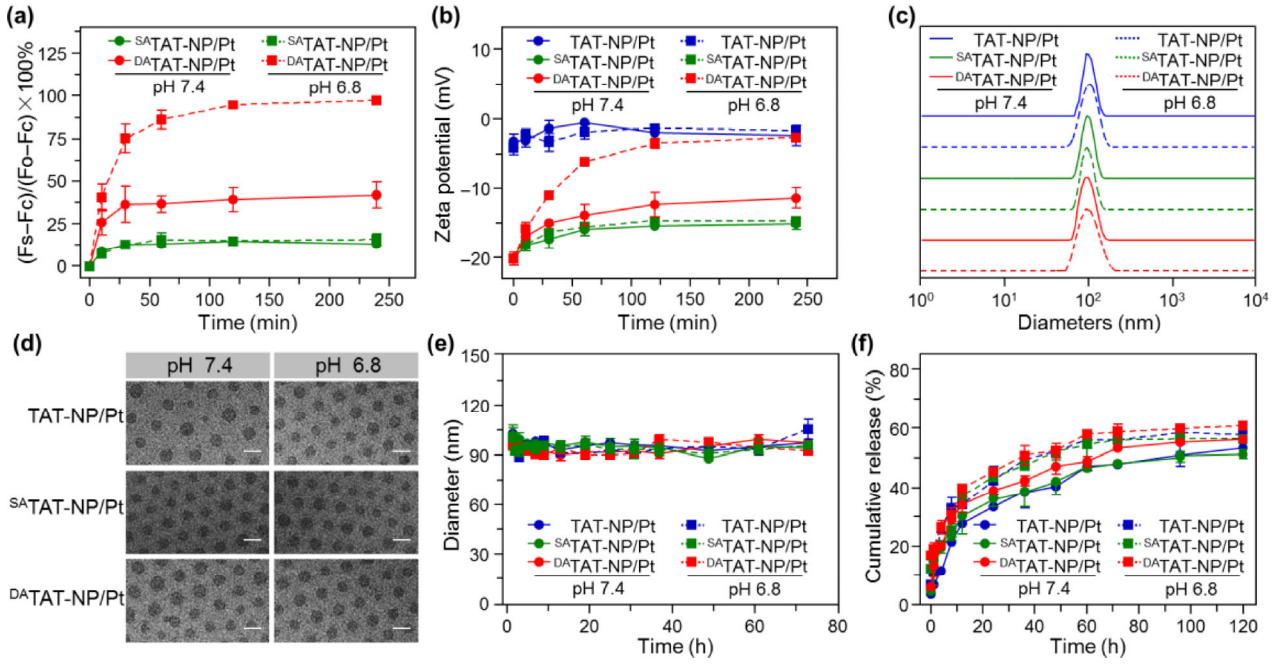

Figure 2 Characterization of TAT-NP/Pt, ^{SA}TAT-NP/Pt, and ^{DA}TAT-NP/Pt. (a) Recovery of active TAT peptide at pH 7.4 and 6.8 by quantifying the amount of amines after DA or SA degradation from ^{DA}TAT-NP/Pt and ^{SA}TAT-NP/Pt. Fluorescamine was used as the sensor for amine quantification. (b) Zeta potential changes of TAT-NP/Pt, ^{SA}TAT-NP/Pt, and ^{DA}TAT-NP/Pt at pH 7.4 and 6.8. (c) Hydrodynamic sizes of TAT-NP/Pt, ^{SA}TAT-NP/Pt, and ^{DA}TAT-NP/Pt at pH 7.4 or 6.8 measured by DLS. (d) Cryo-TEM image of TAT-NP/Pt, ^{SA}TAT-NP/Pt, and ^{DA}TAT-NP/Pt at pH 7.4 or 6.8 (scale bar = 100 nm). (e) Diameter changes of NMs after incubation with 10% fetal bovine serum at 37 ˚C at pH 7.4 and 6.8. (f) Release profiles of the platinum drug from TAT-NP/Pt, ^{SA}TAT-NP/Pt, and ^{DA}TAT-NP/Pt at pH 7.4 or 6.8. Data are shown as mean ± SD (n = 3).

of the ^{DA}TAT-NP/Pt only slightly increased to −13.2 mV at pH 7.4, after up to 4 h, confirming its stability under neutral conditions. The two controls, ^{SA}TAT-NP/Pt and TAT-NP/Pt, exhibited negligible changes in zeta potential at either pH 7.4 or 6.8.

Next, the effect of pH on the physicochemical characteristics of these Pt(IV) prodrug-encapsulated nanoparticles was examined. The average sizes of TAT-NP/Pt, ^{SA}TAT-NP/Pt, and ^{DA}TAT-NP/Pt as measured by DLS (Fig. 2(c)) were all ~ 100 nm at both pH 7.4 and 6.8. These NMs exhibited compact and uniform spherical morphology at both pH values (Fig. 2(d)) as observed with cryogenic transmission electron microscopy (Cryo-TEM). In addition, TAT-NP/Pt, ^{SA}TAT-NP/Pt, and ^{DA}TAT-NP/Pt exhibited high stability without aggregation for 72 h under both pH conditions (Fig. 2(e)), which could be because of the steric effect of the PEG corona. The effect of pH on the release of the platinum drug was then further examined. The release of the Pt(IV) prodrug from these NMs was a slow and diffusion-controlled process mainly owing to polymer biodegradation and prodrug diffusion [40, 46]. The mildly acidic condition (pH 6.8) had a negligible effect on the platinum release rate for all three NMs, with approximately ~ 60% of the platinum drug being released by 120 h at either pH 7.4 or 6.8.

Based on the above results, it could be concluded that the slightly lower pH value was capable of triggering the rapid degradation of amide bonds formed between the TAT peptide lysine residue amines and DA, and thereby reactivating the TAT peptide. In contrast, the TAT peptide lysine residue amines modified by SA were stable at pH_e. In addition, the pH value did not affect the size, morphology, stability, or release profile of these NMs, ensuring that the pH_e-activated TAT peptide was the only variable to affect the *in vitro* and *in vivo* performances of the ^{DA}TAT-NP/Pt.

3.2 pH_e-triggered TAT-presenting enhanced the uptake of ^{DA}TAT-NP/Pt by A549R cells

According to our design, the TAT peptide masked by DA would be reactivated at the pH_e to enhance cellular internalization of the ^{DA}TAT-NP/Pt and increase the intracellular platinum concentration [30]. To confirm this hypothesis, cisplatin-resistant A549R cells were incubated with RhoB-labeled TAT-NP/Pt, ^{SA}TAT-NP/Pt, and ^{DA}TAT-NP/Pt at either pH 7.4 or 6.8 for 4 h, and then the intracellular fluorescence was determined by flow cytometry (Figs. 3(a) and 3(b)). At neutral pH, A549R cells incubated with RhoB-labeled ^{DA}TAT-NP/Pt or ^{SA}TAT-NP/Pt exhibited much weaker intracellular fluorescence as compared to those incubated with TAT-NP/Pt (Fig. 3(a)), indicating that masking the TAT peptide with DA or SA efficiently suppressed the transmembrane transport function of the TAT peptide. Furthermore, cells incubated with ^{DA}TAT-NP/Pt at pH 6.8 had much stronger intracellular fluorescence, which was comparable to the cells treated with TAT-NP/Pt (Fig. 3(b)). Enhanced cellular uptake of ^{DA}TAT-NP/Pt at pH_e was further corroborated by CLSM. As shown in Fig. 3(c), the cellular fluorescence intensity of ^{DA}TAT-NP/Pt at pH 6.8 was much stronger than that at pH 7.4, while the pH value had a negligible effect the cellular uptake of TAT-NP/Pt and ^{SA}TAT-NP/Pt. Enhanced cellular uptake of the ^{DA}TAT-NP/Pt could be attributed to the reactivated cell penetrating capacity of the TAT peptide triggered by the pH_e, which in turn promoted its internalization into tumor cells. In contrast, this phenomenon was not observed for the ^{SA}TAT-NP/Pt because the TAT peptide modified with SA was stable at pH_e.

Enhanced cellular uptake of ^{DA}TAT-NPs/Pt at pH_e should be accompanied by increased intracellular platinum concentration. To further confirm this hypothesis, A549R cells were cultured with TAT-NP/Pt, ^{SA}TAT-NP/Pt, and ^{DA}TAT-NP/Pt at pH 7.4 or 6.8 for different periods of time, and then, the intracellular platinum contents were determined by ICP-MS, normalized to cell numbers. As shown in Fig. 3(d), extension of the incubation time, and thus, reactivation of TAT peptide at the pH_e resulted in dramatically more intracellular platinum for cells incubated with ^{DA}TAT-NP/Pt. In particular, the amount of platinum doubled (394.3 ng for 1 × 10^6 cells) incubated at pH 6.8 as compared to those incubated at pH 7.4 (196.5 ng for 1 × 10^6 cells) after 4 h of co-incubation with ^{DA}TAT-

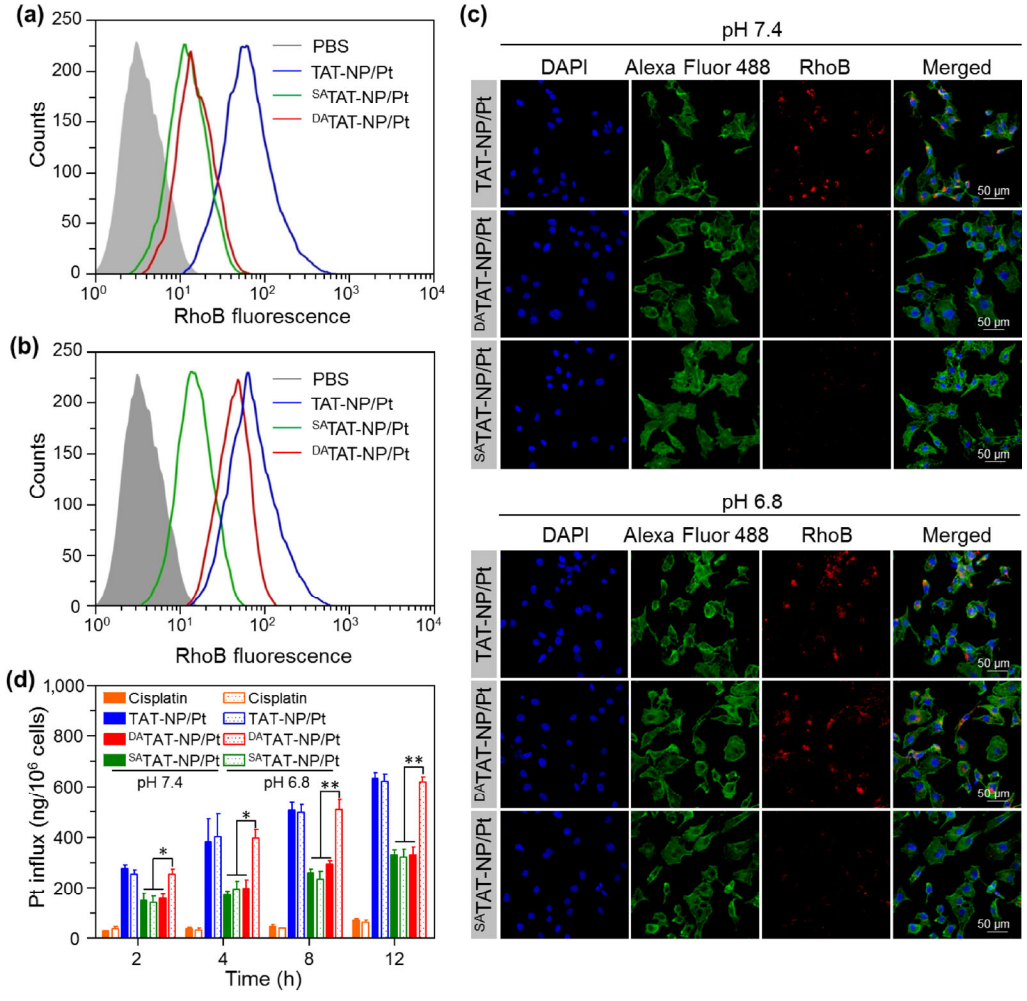

Figure 3 The cellular uptake of TAT-NP/Pt, ^{SA}TAT-NP/Pt, and ^{DA}TAT-NP/Pt at pH 7.4 and 6.8. (a) and (b) Flow cytometry analysis of A549R cells after incubation with RhoB-labeled TAT-NP/Pt, ^{SA}TAT-NP/Pt, and ^{DA}TAT-NP/Pt at (a) pH 7.4 and (b) 6.8. (c) CLSM observation of A549R cells incubated with RhoB-labeled ^{DA}TAT-NP/Pt, ^{SA}TAT-NP/Pt, and TAT-NP/Pt (red) for 4 h at pH 7.4 and 6.8. The cytoskeleton and cell nuclei were stained by Alexa Fluor 488 (green) and DAPI (blue), respectively. (d) Quantitative analysis of intracellular platinum contents determined by ICP-MS. The A549 cells were incubated with cisplatin, TAT-NP/Pt, ^{SA}TAT-NP/Pt, and ^{DA}TAT-NP/Pt at pH 7.4 or 6.8 for 2, 4, 8, and 12 h at an equivalent platinum amount of 50 μM. *$p < 0.05$, **$p < 0.01$.

NP/Pt. In contrast, for cells incubated with ^{SA}TAT-NP/Pt, TAT-NP/Pt, and cisplatin, the amount of intracellular platinum was not affected by the acidic condition of the culture medium. Gradually enhanced intracellular platinum content was observed with prolonged incubation time, suggesting an efficient internalization of NMs, because DA detachment and TAT peptide reactivation required extended reaction time. It is worth mentioning that we also found that these NMs could prevent Pt from the efflux of transport pump (e.g., P-glycoprotein) [47] as evidenced by a much slower Pt efflux rate (Fig. S6 in the ESM).

3.3 pH_e-triggered TAT-presentation facilitated the nuclear translocation of ^{DA}TAT-NP/Pt and increased Pt-DNA adducts in A549R cells

It has been reported that the TAT peptide can bind to NPCs, which quickly translocate the cargo into the perinuclear region [48, 49]. To investigate pH_e-activated nuclear translocation capability of TAT peptide-modified NMs, A549R cells were incubated with RhoB-labeled TAT-NP/Pt, ^{SA}TAT-NP/Pt, and ^{DA}TAT-NP/Pt at pH 6.8 for 10 h, and then the intracellular localization of these NMs was observed by CLSM (Figs. 4(a) and 4(b)). It could be calculated that the

red fluorescence of TAT-NP/Pt was more intense at the periphery of DAPI-labeled cell nuclei most likely because of the TAT-peptide binding to the NPCs. Interestingly, the RhoB fluorescence of ^{DA}TAT-NP/Pt was located around the perinuclear region as well. In contrast, the majority of the red fluorescence for ^{SA}TAT-NP/Pt was confined to the cytoplasm. Furthermore, to precisely quantify the localization of these NMs, the region 5 μm from the nucleus was defined as the perinuclear layer (Fig. 4(a)). Subsequently, the fluorescence intensity of the perinuclear layer and the total intracellular fluorescence intensity were denoted as I_1 and I_2, respectively. The value obtained from dividing I_1 by (I_2 – I_1) was used to evaluate the relative fluorescence intensity of the perinuclear layer. The statistical analysis (Fig. 4(c)) showed that the reactivated TAT peptide of the ^{DA}TAT-NP/Pt facilitated their nuclear targeting and accumulation, while this phenomenon was not observed in the cells incubated with ^{SA}TAT-NP/Pt. This finding essentially revealed that the TAT peptide played a vital role in nuclear translocation.

The enhanced cellular uptake and facilitated nuclear targeting of the ^{DA}TAT-NP/Pt at pH_e should subsequently be accompanied by increased binding with nuclear DNA to form Pt-DNA adducts to exert their anticancer activity. The reduction of Pt(IV) to Pt(II), in concert with the loss of two ligands, is essential to palatinate DNA [50]. The Pt(IV) prodrug can be reduced to free Pt(II) under the cellular reductive conditions, and thus the free Pt(II) is released into the cytoplasm. We verified this by quantifying the ratio of cellular Pt(IV) to Pt(II) using X-ray photoelectron spectroscopy (XPS) at different incubation times (Fig. S7 in the ESM). Analyses of Pt 4f XPS peaks (Fig. S8 in the ESM) clearly showed that the ratio of

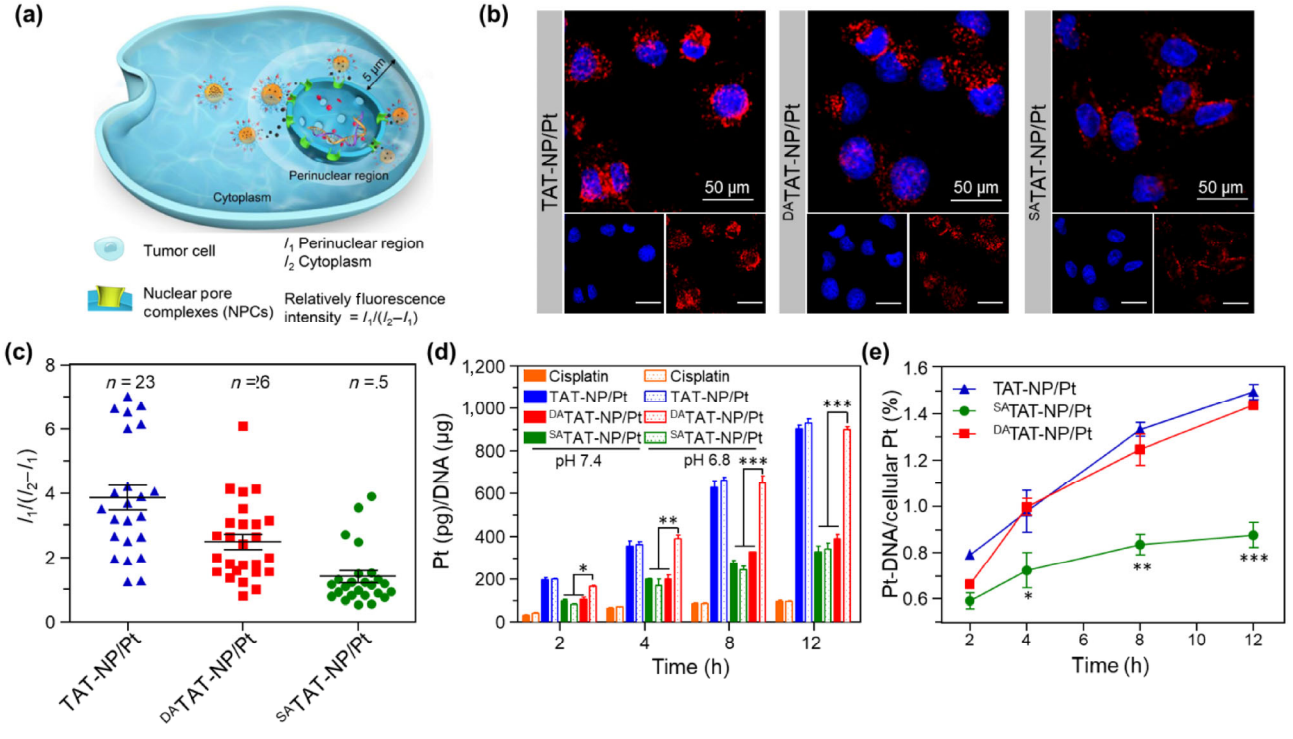

Figure 4 (a) Schematic showing that cellular distribution of NMs. The region of cell between the nucleus and cell membrane was defined as the cytoplasmic region. The cytoplasmic region surrounding the nucleus that is 5 μm away from the nuclear membrane was defined as the perinuclear region. (b) CLSM observation of A549R cells incubated with RhoB-labeled TAT-NP/Pt, ^{SA}TAT-NP/Pt, and ^{DA}TAT-NP/Pt (red) at pH 6.8. The cells were stained with DAPI (blue) for the cell nucleus. (c) Statistical analysis of relative fluorescence intensity between the perinuclear region and the cytoplasmic region, and *n* is the number of cells in the statistics. (d) Quantification of Pt-DNA adducts. A549R cells were treated with cisplatin, TAT-NP/Pt, ^{SA}TAT-NP/Pt, and ^{DA}TAT-NP/Pt at an equivalent platinum amount of 50 μM for 2, 4, 8, and 12 h, respectively. $^{**}p < 0.01$, $^{***}p < 0.001$. (e) The ratio of platinum in Pt-DNA adducts and total cellular platinum at 2, 4, 8, and 12 h at pH 6.8, respectively. $^{*}p < 0.05$, $^{**}p < 0.01$, $^{***}p < 0.001$.

the divalent form increased with incubation time, indicating the release of Pt(IV) and the generation of active Pt(II). The formation of Pt-DNA adducts was further quantitatively determined. As shown in Fig. 4(d), the Pt-DNA adducts in cisplatin-resistant A549R cells after treatment with ^{DA}TAT-NP/Pt were 3.9-fold, 5.5-fold, 7.6-fold, and 10.5-fold more than that of free cisplatin at 2, 4, 8, and 12 h, respectively. Moreover, the amount of platinum in the DNA following incubation with ^{DA}TAT-NP/Pt at pH 6.8 was higher than in the DNA of cells treated with ^{DA}TAT-NP/Pt at pH 7.4, reaching a level comparable to that of TAT-NP/Pt at pH 7.4 or 6.8. In contrast, the ^{SA}TAT-NP/Pt exhibited a relatively smaller amount of Pt-DNA adducts at both pH values at each corresponding time point. This could be attributed to the limited internalization and nuclear translocation of the SA-masked TAT peptide. Furthermore, the ratio of platinum in the nucleus vs. the cytoplasm was calculated by normalizing the amount of platinum in Pt-DNA adducts to that in cells treated under the same conditions. As shown in Fig. 4(e), ^{DA}TAT-NP/Pt and TAT-NP/Pt treated groups exhibit higher nucleus-to-cytoplasm ratios regarding the amount of platinum at each time point. ^{DA}TAT-NP/Pt exhibited closer perinuclear distribution while similar Pt release (Fig. 2(f)) compared to ^{SA}TAT-NP/Pt, resulted in higher amount of Pt in the nuclei, which proved the critical role of nucleus translocation of NMs. Thus, we demonstrated that the reactivated TAT peptide at pH_e enhanced cellular uptake and facilitated nuclear targeting, resulting in a significant increase in the levels of Pt-DNA adducts.

3.4 pH_e-triggered TAT-presentation circumvented cisplatin resistance *in vitro*

The increased cellular Pt-DNA adduct formation of ^{DA}TAT-NP/Pt at pH_e should subsequently trigger an elevated amount of cell apoptosis in the cisplatin-resistant A549R cells [51]. To verify this, A549R cells were treated with the aforementioned formulations for 6 h at either pH 7.4 or 6.8. The cells were further incubated in fresh culture medium at pH 7.4 for 42 h and then stained with Annexin-V-FITC and propidium iodide (PI) to quantify cell apoptosis and necrosis. The FACS results in Fig. 5(a) demonstrated that treatment with the ^{DA}TAT-NP/Pt induced apoptosis in 69.4% of A549R cells, which was 3.9-fold more than that of the cisplatin alone treatment at pH 6.8, while only 42.0% of the population was apoptotic when A549R cells were treated with ^{DA}TAT-NP/Pt at pH 7.4. Moreover, the ^{SA}TAT-NP/Pt did not remarkably enhance cell apoptosis at either pH 7.4 or 6.8, only leading to the level similar to that induced by ^{DA}TAT-NP/Pt at pH 7.4.

Furthermore, to evaluate the efficacy of ^{DA}TAT-NP/Pt for overcoming cisplatin resistance, its antiproliferative efficiency against cisplatin-resistant A549R cells was tested by the MTT assay. After treatment with the aforementioned formulations for 6 h at either pH 7.4 or 6.8, the A549R cells were further incubated with fresh medium at pH 7.4 for 66 h, and then the half-maximal inhibitory concentration (IC_{50}) values of these formulations were calculated according to the MTT results. As shown in Figs. 5(b) and 5(c), the IC_{50} value of the ^{DA}TAT-NP/Pt treatment in A549R cells was 5.3 μM at pH 6.8, which was significantly lower than that at pH 7.4 (IC_{50} = 27.6 μM). However, there were no significant differences when A549R cells were treated with cisplatin (84.1 μM at pH 6.8 to 84.3 μM at pH 7.4), ^{SA}TAT-NP/Pt (22.4 μM at pH 6.8 to 25.9 μM at pH 7.4), or TAT-NP/Pt (5.1 μM at pH 6.8 to 8.1 μM at pH 7.4) at pH 6.8 and 7.4. At high concentrations of Pt (> 50 μM), nearly all the cells were dead and the growth inhibition rates were indistinguishable. Based on the above *in vitro* results, it could be concluded that the reactivated TAT peptide at pH_e enhanced cellular internalization and facilitated perinuclear translocation of the ^{DA}TAT-NP/Pt in cisplatin-resistant A549R cells. Therefore, with the increase in Pt-DNA adducts, the level of apoptosis of A549R cells was remarkably elevated, resulting in the circumvention of cisplatin resistance *in vitro*.

3.5 pH_e-triggered TAT-presentation augmented tumor accumulation and retention *in vivo*

We further studied the tumor accumulation and retention of ^{DA}TAT-NP/Pt *in vivo*. The pharmacokinetics and biodistribution of these NMs in mice were examined. After intravenous injection of cisplatin,

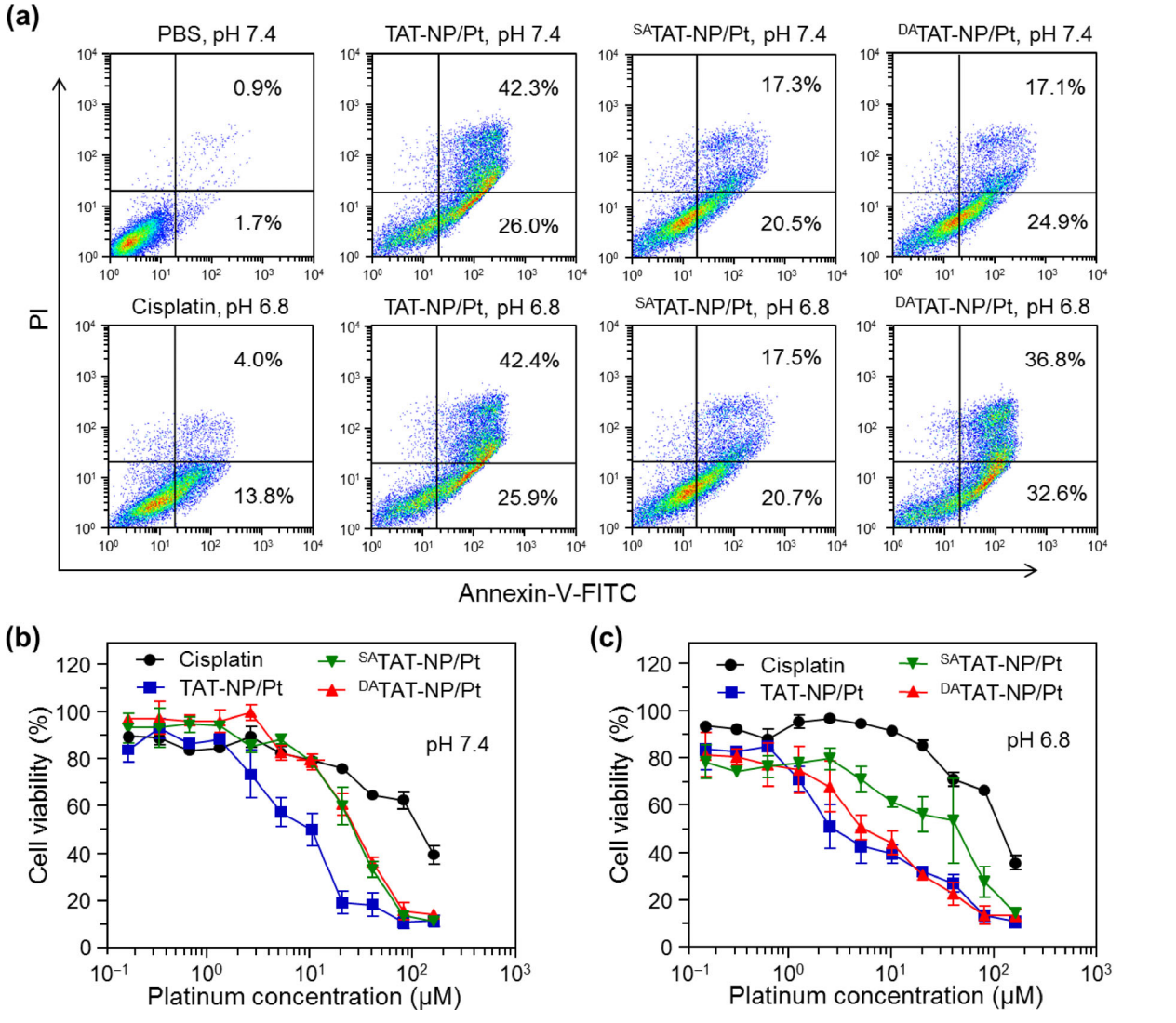

Figure 5 (a) Apoptosis induced by cisplatin, TAT-NP/Pt, ^{SA}TAT-NP/Pt, and ^{DA}TAT-NP/Pt in A549R cells. Annexin V-FITC/PI staining detects apoptosis in cells after treatment for 6 h and fresh medium for another 42 h at pH 7.4 or 6.8. The bottom-right panel presents early apoptotic cells, while the top-right panel displays late apoptotic cells. (b) and (c) Viability of A549R cells after a 6 h incubation with the indicated formulations at (b) pH 7.4 or (c) pH 6.8 and further 66 h incubation with fresh medium. Data are shown as mean ± SD (n = 3).

TAT-NP/Pt, ^{SA}TAT-NP/Pt, or ^{DA}TAT-NP/Pt at a dose of 2.0 mg of platinum per kg of mouse body weight, blood samples of NOD/SCID mice were collected at predetermined time points, and the platinum content in plasma was analyzed using ICP-MS. The curves representing the percentage of injected platinum that remained in the plasma versus time (post-administration) were shown in Fig. 6(a), and the pharmacokinetic parameters were presented in Table S1 (in the ESM) using a non-compartmental model. ^{DA}TAT-NP/Pt and ^{SA}TAT-NP/Pt exhibited similar pharmacokinetics, and exhibited a prolonged half-life in circulating blood as compared to TAT-NP/Pt. The C_{max} and AUC_{0-48h} of the ^{DA}TAT-NP/Pt in the plasma were 3.3-fold and 4.6-fold higher than those of the TAT-NP/Pt, respectively. The blood clearance of the ^{DA}TAT-NP/Pt (6.7 L·h^{-1}·kg^{-1}) was much slower than that of the TAT-NP/Pt (29.0 L·h^{-1}·kg^{-1}). Therefore, masking the TAT peptide made ^{DA}TAT-NP/Pt less accessible by RES, achieving prolonged circulation, which provided more opportunities for encapsulated platinum to accumulate in tumor sites.

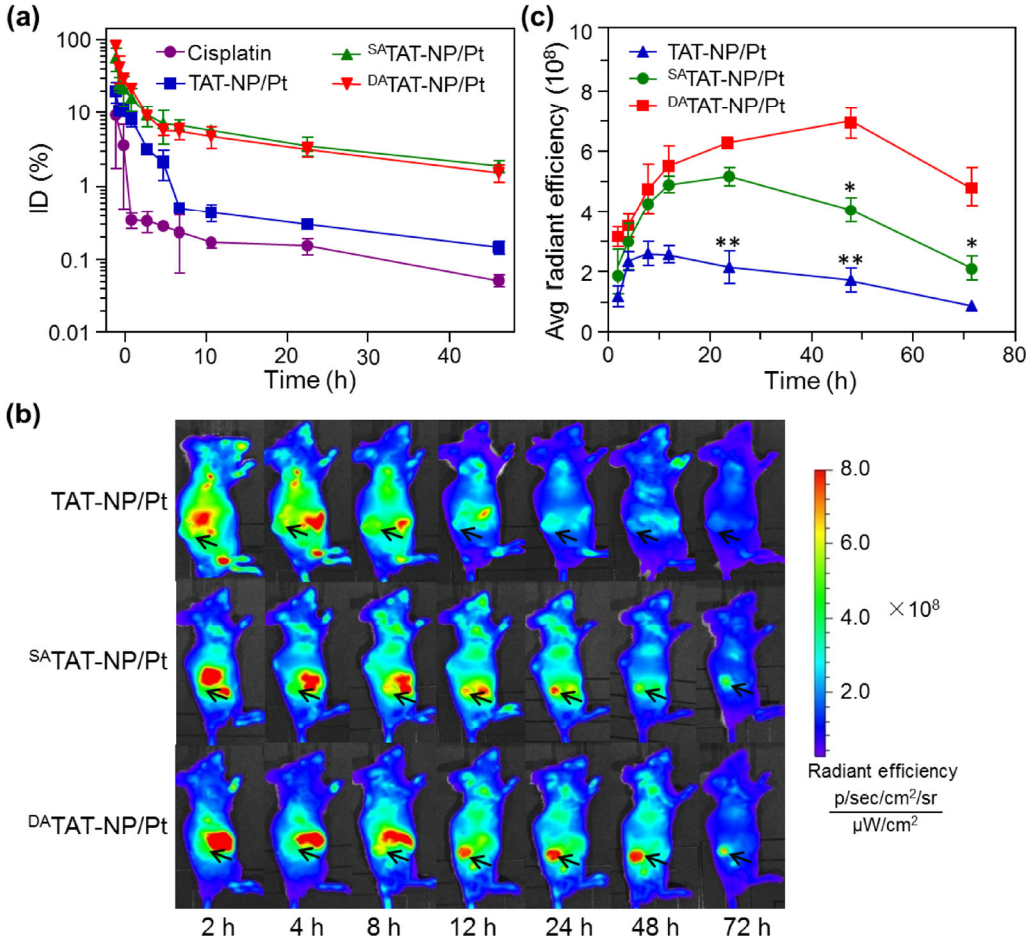

Figure 6 (a) Pharmacokinetics of cisplatin, TAT-NP/Pt, ^{SA}TAT-NP/Pt, and ^{DA}TAT-NP/Pt after i.v. administration (mean ± SD, n = 4). (b) *In vivo* time-dependent fluorescence images of A549R tumor-bearing mouse. Black arrows indicate tumor sites. (c) Cy5.5 fluorescence intensity in the tumor region collected at 2, 4, 8, 12, 24, 48, and 72 h following systemic injection. *p < 0.05, **p < 0.01, ***p < 0.001.

Subsequently, the biodistribution and accumulation of the ^{DA}TAT-NP/Pt in tumor tissues was determined. Cy5.5-labeled NMs were intravenously injected into mice with A549R xenografts, and then the whole mouse was imaged with Xenogen IVIS® Lumina system. As shown in Fig. 6(b), the highest fluorescence intensity of Cy5.5 was found in the ^{DA}TAT-NP/Pt in tumor tissues followed by ^{SA}TAT-NP/Pt, and TAT-NP/Pt, indicating the outstanding capacity of ^{DA}TAT-NP/Pt to enhance drug accumulation and retention in the tumor site. The accumulation of Cy5.5-labeled ^{DA}TAT-NP/Pt were 2.8-fold, 3.9-fold, and 6.3-fold more than that of TAT-NP/Pt at 24, 48, and 72 h, respectively. Moreover, after treatment with ^{DA}TAT-NP/Pt, the fluorescence intensity of Cy5.5 continually increased at the tumor site over the first 24 h, and a similar trend of fluorescence change was observed for ^{SA}TAT-NP/Pt, even though the mean fluorescence intensity of the latter was less. Subsequently, for the ^{DA}TAT-NP/Pt group, the fluorescence in tumor tissue gradually increased over 48 h, and then slowly decayed. In contrast, the fluorescent signal in the tumor tissue rapidly decayed at 24 h after treatment with the ^{SA}TAT-NP/Pt, suggesting less retention in tumors. TAT-NP/Pt exhibited even faster tumor clearance with a fluorescence decrease time at 8 h, owing to its inferior blood circulation behavior.

In addition, at 24, 48, and 72 h post-injection of the TAT-NP/Pt, ^{DA}TAT-NP/Pt, or ^{SA}TAT-NP/Pt, the mice were sacrificed and major organs and tumor tissues were collected for Xenogen IVIS® Lumina system analysis (Fig. S9 in the ESM). The majority of Cy5.5

fluorescence was distributed in the kidney, liver, and lung, which were respectively responsible for clearing, processing, and degrading foreign material from blood circulation [52]. Furthermore, in the tumor tissues, the Cy5.5 fluorescence intensity from the NMs decreased in the order of ^{DA}TAT-NP/Pt > ^{SA}TAT-NP/Pt > TAT-NP/Pt, which was consistent with the above results (Figs. 6(b) and 6(c)). It is reasonable that the lowest accumulation of TAT-NP/Pt in the tumor tissue resulted from the rapid clearance from the blood (Fig. 6(a)). However, it is unexpected that ^{DA}TAT-NP/Pt exhibited much stronger tumor accumulation than treatment with ^{SA}TAT-NP/Pt, given the fact that these two NMs showed comparable pharmacokinetics and were expected to possess similar tumor accumulation [53]. Thus, the reactivation of the TAT peptide on ^{DA}TAT-NP/Pt by tumor acidity should play a critical role during tumor accumulation and retention.

To further elucidate the mechanism underlying enhanced tumor accumulation and retention of pH_e-activatable NMs, we used a microfluidic channel loading tumor-like A549R multicellular spheroids (MCSs) to simulate a tumor undergoing physiological flow flushing and study its interaction with NMs under such conditions. Flushing the spheroids with medium containing NMs or fresh medium can be used to assess tumor accumulation and retention, respectively. The microfluidic device was mounted on a microscope stage (Fig. 7(a)), and the fluorescence intensity and distribution inside the MCSs were imaged using the 20× objective with a 546-nm excitation wavelength on a confocal microscope. The flow rate of the device was controlled at 450 $\mu L \cdot h^{-1}$ by a syringe pump, which is similar to interstitial flow inside a tumor [18, 54]. A549R MCSs, embedded in an ECM forming a network mimicking the interstitial spaces of tumor tissue, were gently loaded into the microfluidic device. Subsequently, RhoB-labeled TAT-NP/Pt, ^{SA}TAT-NP/Pt, and ^{DA}TAT-NP/Pt pre-incubated in flowing media at pH 6.8 for 4 h were added, respectively, as the continuous flow. The accumulation of NMs in A549R MCSs was then quantified at different time points (Fig. S10 in the ESM). The TAT-modified NM produced a 2.3-fold mean fluorescence intensity increase in the accumulation of TAT-NP/Pt relative to ^{SA}TAT-NP/Pt with a non-pH_e-responsive SA-masked TAT peptide after an influx of 60 min. The reactivation of the TAT peptide at pH 6.8 produced similar accumulation kinetics for ^{DA}TAT-NP/Pt with TAT-NP/Pt, indicating the fast recovery of the TAT peptide at pH_e (Fig. 7(b)). The results showed that NMs modified with the TAT peptide can be released from the matrix, as is evident by the increase in fluorescence of NMs in the center of spheroids with time. Flushing MCSs with fresh medium without NMs produced an approximately 90% decrease in the spheroid fluorescence for ^{SA}TAT-NP/Pt within 1 h, which implied that most ^{SA}TAT-NP/Pt diffused into the surrounding and its efflux from the spheroid occurred rapidly (Figs. 7(c)–7(e)). In contrast, the retention of both ^{DA}TAT-NP/Pt and TAT-NP/Pt in MCSs was dramatically improved with much slower tumor efflux, suggesting that the TAT peptide can prevent flushing by external fluids. Fluorescent distribution of TAT-NP/Pt, ^{SA}TAT-NP/Pt, and ^{DA}TAT- NP/Pt in spheroids (the corresponding fluorescence vs. radial depths) at 30 and 120 min time points (Figs. 7(d) and 7(e)) further confirmed the conclusion above. These results were in agreement with the above *in vivo* studies and further suggested that the reactivation of the TAT peptide was able to enhance interactions between NMs with tumor cells and the ECM matrix, thereby leading to the increased accumulation and retention in tumor tissue.

3.6 pH_e-triggered TAT-presentation efficiently overcame cisplatin resistance *in vivo*

Encouraged by the capacity of ^{DA}TAT-NP/Pt to circumvent cisplatin-resistant tumor cells, we then performed animal experiments to further confirm our hypothesis *in vivo*. NOD/SCID mice with A549R xenografts were intravenously injected with cisplatin, TAT-NP/Pt, ^{SA}TAT-NP/Pt, or ^{DA}TAT-NP/Pt at a dose of 2.0 mg of platinum per kg of mouse body weight. Mice injected with PBS or blank nanoparticles (^{DA}TAT-NP) were used as negative controls. The treatments were repeated three times at a time interval of 6 days (Fig. 8(a)). The tumor volume and body mass were monitored during the duration of the study. As shown in Fig. 8(b), administration of free cisplatin and TAT-NP/Pt only resulted in ~ 40% inhibition of tumor growth, while treatment with ^{SA}TAT-NP/Pt showed ~ 60% growth inhibition. However, treatment with

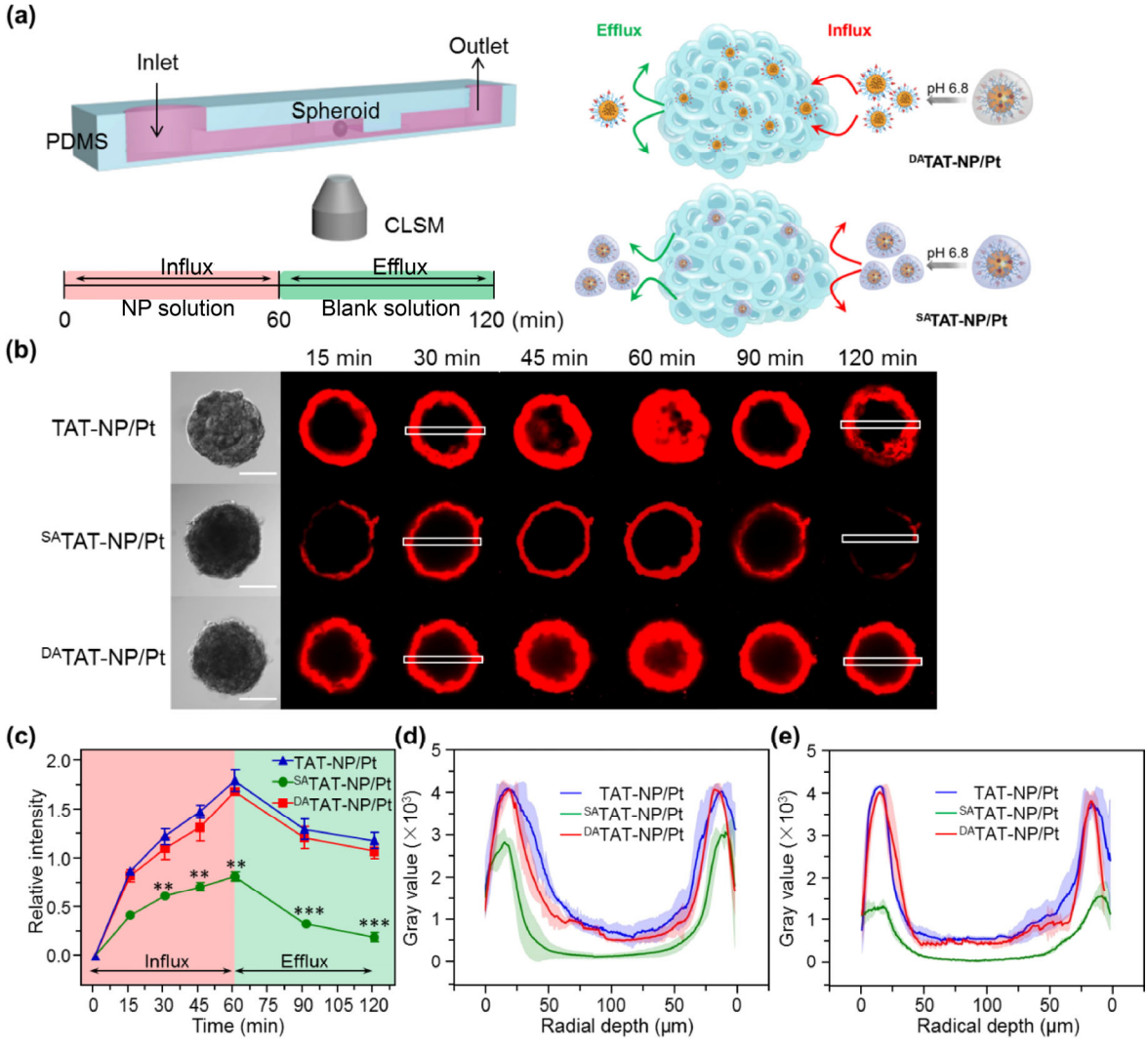

Figure 7 (a) Schematic illustration of a microfluidic device on a microscope stage (left), and the schematic of the fluorescently-labeled ^{DA}TAT-NP/Pt (top-right) and ^{SA}TAT-NP/Pt (bottom-right) administered entering the spheroid and accumulating in the interstitial spaces after pre-incubation at pH 6.8 for 4 h. (b) Mean fluorescence intensity (MFI) of spheroids treated with RhoB labeled TAT-NP/Pt, ^{SA}TAT-NP/Pt, and ^{DA}TAT-NP/Pt at a flow of 450 μL·h^{-1}. These NMs were pre-incubated in a buffer at pH 6.8 for 4 h before being loaded. $^{**}p < 0.01$, $^{***}p < 0.001$. (c) Intensity images of TAT-NP/Pt, ^{SA}TAT-NP/Pt, and ^{DA}TAT-NP/Pt in spheroids under a flow of 450 μL·h^{-1} at a preset time, and fresh image solvent for 60–120 min. (Scale bars, 100 μm). (d) MFI at various radial distances in spheroids treated with TAT-NP/Pt, ^{SA}TAT-NP/Pt, and ^{DA}TAT-NP/Pt at 450 μL·h^{-1} for 30 min, respectively. (e) MFI at various radial distances in spheroids treated with free medium at 450 μL·h^{-1} for 60 min (i.e., at 120 min post time 0). (Data are presented as mean intensity ± SD, $n = 3$).

^{DA}TAT-NP/Pt led to the most pronounced inhibition of tumor growth with an 80% inhibition as well as delayed tumor development (Table S2 in the ESM). On day 22 after the first treatments, tumors in different groups were harvested, weighed, and photographed. Tumor weights and direct observation of tumors further proved that the antitumor efficacy was improved markedly for the ^{DA}TAT-NP/Pt group (Figs. 8(c) and 8(d)). Additionally, hematoxylin and eosin (H&E) staining showed that tumor cells treated with ^{DA}TAT-NP/Pt had apparent nuclei deficiency, compared with those treated with PBS (Fig. S11 in the ESM), suggesting that a massive number of tumor cells were apoptotic or necrotic. Meanwhile, immunohistochemical studies also confirmed the improved therapeutic effect of ^{DA}TAT-NP/Pt, showing a reduction

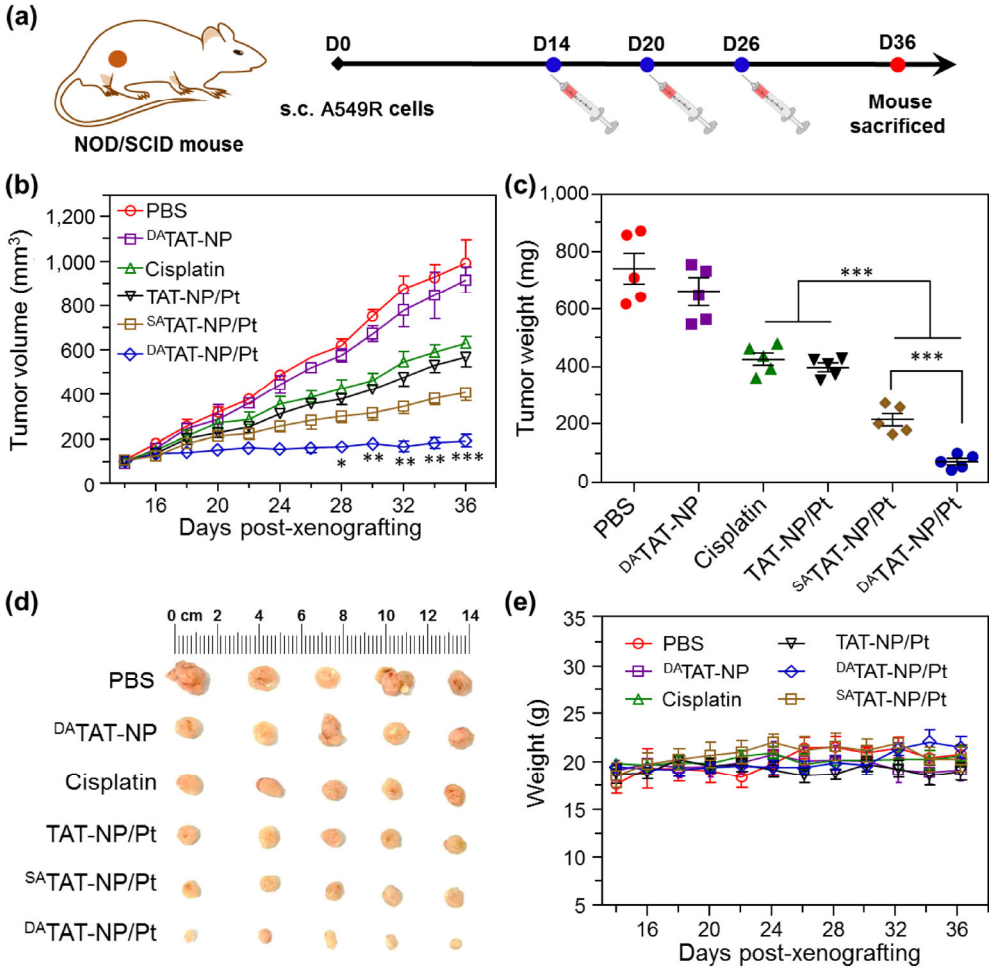

Figure 8 Anti-tumor activities of different formulations in A549R tumor-bearing mice. (a) Treatment schedule for ^{DA}TAT-NP/Pt of NOD/SCID mice bearing A549R tumors. (b)Tumor volume changes after injections of PBS, ^{DA}TAT-NP, cisplatin, TAT-NP/Pt, ^{SA}TAT-NP/Pt, and ^{DA}TAT-NP/Pt at day 14, 20, and 26 post-xenografting. The red arrows indicate injection date. *$p < 0.05$, **$p < 0.01$, ***$p < 0.001$. (c) Tumor weight of A549R tumors at the day 36 post-xenografting. (d) Tumor images at the day 36 post-xenografting. (e) Body weight monitoring for the mice receiving different formulation treatments. Data are shown as mean ± SD ($n = 5$).

in proliferation and an increase in the apoptosis of tumor cells. No significant body weight fluctuations were observed in any of the groups (Fig. 8(e)). In addition, systemic administration of these NMs in mice induced negligible damage to the liver, kidney, or spleen according to the H&E staining results (Fig. S12 in the ESM), with the exception of kidney tissues in the cisplatin-treated group that showed nephrotoxicity via the appearance of tubular injury.

4 Conclusion

In summary, we demonstrated that a TAT ligand-presenting hierarchical targeting strategy can, apart from improving tumor accumulation and cell uptake, integrate the advantages of both preferable tumor retention and enhanced nuclear translocation of NMs. This design possessed several distinct advantages to combat the sequential drug delivery barriers. First, the TAT peptide masked with DA could avoid rapid clearance by blood circulation and efficiently enter into tumor tissue. Second, the masked TAT peptide of ^{DA}TAT-NP/Pt was reactivated at pH_e by the cleavage of amide bonds followed by the recovery of the cell penetrating TAT peptide. The reactivated ^{DA}TAT-NP/Pt enhanced the interaction between NMs and cells, and prevented efflux by fluid flow. Third, it facilitated tumor cell internalization and quickly translocated

platinum into the perinuclear region and cell nucleus, which resulted in significantly increased Pt-DNA adducts, thereby sensitizing the drug-resistant cells to chemotherapy. This strategy provides a simple and highly applicable strategy to overcome drug delivery barriers and is promising for future clinical applications.

Acknowledgements

This work was supported by the National Key R&D Program of China (No. 2017YFA0205600), and the National Natural Science Foundation of China (Nos. 51773191, 51573176 and 51633008).

Electronic Supplementary Material: Supplementary material (^{1}H NMR spectra and GPC spectra of polymers, immunohistochemical analysis, the distribution of nanoparticles *ex vivo,* z-stack images of tumor spheroids) is available in the online version of this article at https://doi.org/10.1007/s12274-017-1925-4.

References

[1] Shi, J. J.; Kantoff, P. W.; Wooster, R.; Farokhzad, O. C. Cancer nanomedicine: Progress, challenges and opportunities. *Nat. Rev. Cancer* **2017**, *17*, 20–37.

[2] Davis, M. E.; Chen, Z.; Shin, D. M. Nanoparticle therapeutics: An emerging treatment modality for cancer. *Nat. Rev. Drug Discov.* **2008**, *7*, 771–782.

[3] Wang, J. Q.; Mao, W. W.; Lock, L. L.; Tang, J. B.; Sui, M. H.; Sun, W. L.; Cui, H. G.; Xu, D.; Shen, Y. Q. The role of micelle size in tumor accumulation, penetration, and treatment. *ACS Nano* **2015**, *9*, 7195–7206.

[4] Byrne, J. D.; Betancourt, T.; Brannon-Peppas, L. Active targeting schemes for nanoparticle systems in cancer therapeutics. *Adv. Drug. Deliv. Rev.* **2008**, *60*, 1615–1626.

[5] Schrama, D.; Reisfeld, R. A.; Becker, J. C. Antibody targeted drugs as cancer therapeutics. *Nat Rev. Drug Discov.* **2006**, *5*, 147–159.

[6] Lu, Y.; Aimetti, A. A.; Langer, R.; Gu, Z. Bioresponsive materials. *Nat. Rev. Mater.* **2016**, *2*, 16075.

[7] Wang, T. T.; Wang, D. G.; Liu, J. P.; Feng, B.; Zhou, F. Y.; Zhang, H. W.; Zhou, L.; Yin, Q.; Zhang, Z. W.; Cao, Z. L. et al. Acidity-triggered ligand-presenting nanoparticles to overcome sequential drug delivery barriers to tumors. *Nano Lett.* **2017**, *17*, 5429–5436.

[8] Torchilin, V. P. Multifunctional, stimuli-sensitive nanoparticulate systems for drug delivery. *Nat. Rev. Drug Discov.* **2014**, *13*, 813–827.

[9] Mura, S.; Nicolas, J.; Couvreur, P. Stimuli-responsive nanocarriers for drug delivery. *Nat. Mater.* **2013**, *12*, 991–1003.

[10] Mo, R.; Jiang, T. Y.; DiSanto, R.; Tai, W. Y.; Gu, Z. Atp-triggered anticancer drug delivery. *Nat. Commun.* **2014**, *5*, 3364.

[11] Ji, T. J.; Lang, J. Y.; Wang, J.; Cai, R.; Zhang, Y. L.; Qi, F. F.; Zhang, L. J.; Zhao, X.; Wu, W. J.; Hao, J. H. et al. Designing liposomes to suppress extracellular matrix expression to enhance drug penetration and pancreatic tumor therapy. *ACS Nano* **2017**, *11*, 8668–8678.

[12] Liu, Y.; van der Mei, H. C.; Zhao, B. R.; Zhai, Y.; Cheng, T. J.; Li, Y. F.; Zhang, Z. K.; Busscher, H. J.; Ren, Y. J.; Shi, L. Q. Eradication of multidrug-resistant staphylococcal infections by light-activatable micellar nanocarriers in a murine model. *Adv. Funct. Mater.* **2017**, *27*, 1701974.

[13] Du, B. J.; Liu, J. H.; Ding, G. Y.; Han, X.; Li, D.; Wang, E. K.; Wang, J. Positively charged graphene/fe3o4/polyethylenimine with enhanced drug loading and cellular uptake for magnetic resonance imaging and magnet-responsive cancer therapy. *Nano Res.* **2017**, *10*, 2280–2295.

[14] Wang, S.; Huang, P.; Chen, X. Y. Hierarchical targeting strategy for enhanced tumor tissue accumulation/retention and cellular internalization. *Adv. Mater.* **2016**, *28*, 7340–7364.

[15] Tang, L.; Yang, X. J.; Yin, Q.; Cai, K. M.; Wang, H.; Chaudhury, I.; Yao, C.; Zhou, Q.; Kwon, M.; Hartman, J. A. et al. Investigating the optimal size of anticancer nanomedicine. *Proc. Natl. Acad. Sci. USA* **2014**, *111*, 15344–15349.

[16] Larsen, E. K. U.; Nielsen, T.; Wittenborn, T.; Birkedal, H.; Vorup-Jensen, T.; Jakobsen, M. H.; Ostergaard, L.; Horsman, M. R.; Besenbacher, F.; Howard, K. A. et al. Size-dependent accumulation of pegylated silane-coated magnetic iron oxide nanoparticles in murine tumors. *Acs Nano* **2009**, *3*, 1947–1951.

[17] Zhang, D.; Qi, G. B.; Zhao, Y. X.; Qiao, S. L.; Yang, C.; Wang, H. *In situ* formation of nanofibers from purpurin18-peptide conjugates and the assembly induced retention effect in tumor sites. *Adv. Mater.* **2015**, *27*, 6125–6130.

[18] Albanese, A.; Lam, A. K.; Sykes, E. A.; Rocheleau, J. V.; Chan, W. C. W. Tumour-on-a-chip provides an optical window into nanoparticle tissue transport. *Nat. Commun.* **2013**, *4*, 2718.

[19] Yameen, B.; Choi, W. I.; Vilos, C.; Swami, A.; Shi, J. J.; Farokhzad, O. C. Insight into nanoparticle cellular uptake and intracellular targeting. *J. Control. Release* **2014**, *190*, 485–499.

[20] Pan, L. M.; Liu, J. N.; He, Q. J.; Wang, L. J.; Shi, J. L. Overcoming multidrug resistance of cancer cells by direct intranuclear drug delivery using TAT-conjugated mesoporous silica nanoparticles. *Biomaterials* **2013**, *34*, 2719–2730.

[21] Holohan, C.; van Schaeybroeck, S.; Longley, D. B.; Johnston, P. G. Cancer drug resistance: An evolving paradigm. *Nat. Rev. Cancer* **2013**, *13*, 714–726.

[22] Meijer, C.; Mulder, N. H.; Timmer-Bosscha, H.; Sluiter, W. J.; Meersma, G. J.; De Vries, E. G. E. Relationship of cellular glutathione to the cytotoxicity and resistance of seven platinum compounds. *Cancer Res.* **1992**, *52*, 6885–6889.

[23] Han, K.; Zhang, W. Y.; Zhang, J.; Lei, Q.; Wang, S. B.; Liu, J. W.; Zhang, X. Z.; Han, H. Y. Acidity-triggered tumor-targeted chimeric peptide for enhanced intra-nuclear photodynamic therapy. *Adv. Funct. Mater.* **2016**, *26*, 4351 Func.

[24] Han, S. S.; Li, Z. Y.; Zhu, J. Y.; Han, K.; Zeng, Z. Y.; Hong, W.; Li, W. X.; Jia, H. Z.; Liu, Y.; Zhuo, R. X. et al. Dual-pH sensitive charge-reversal polypeptide micelles for tumor-triggered targeting uptake and nuclear drug delivery. *Small* **2015**, *11*, 25431 ive.

[25] Xu, P. S.; van Kirk, E. A.; Zhan, Y. H.; Murdoch, W. J.; Radosz, M.; Shen, Y. Q. Targeted charge-reversal nanoparticles for nuclear drug delivery. *Angew. Chem., Int. Ed.* **2007**, *46*, 4999–5002.

[26] Wang, H. B.; Li, Y.; Bai, H. S.; Shen, J.; Chen, X.; Ping, Y.; Tang, G. P. A cooperative dimensional strategy for enhanced nucleus-targeted delivery of anticancer drugs. *Adv. Funct. Mater.* **2017**, *27*, 1700339.

[27] Görlich, D.; Kutay, U. Transport between the cell nucleus and the cytoplasm. *Annu. Rev. Cell Dev. Biol.* **1999**, *15*, 607–660.

[28] Tammam, S. N.; Azzazy, H. M. E.; Lamprecht, A. How successful is nuclear targeting by nanocarriers? *J. Control. Release* **2016**, *229*, 140–153.

[29] Qiu, L. P.; Chen, T.; Öçsoy, I.; Yasun, E.; Wu, C. C.; Zhu, G. Z.; You, M. X.; Han, D.; Jiang, J. H.; Yu, R. Q. et al. A cell-targeted, size-photocontrollable, nuclear-uptake nanodrug delivery system for drug-resistant cancer therapy. *Nano. Lett.* **2015**, *15*, 457–463.

[30] Huang, Y. Z.; Jiang, Y. F.; Wang, H. Y.; Wang, J. X.; Shin, M. C.; Byun, Y.; He, H.; Liang, Y. Q.; Yang, V. C. Curb challenges of the "trojan horse" approach: Smart strategies in achieving effective yet safe cell-penetrating peptide-based drug delivery. *Adv. Drug Deliv. Rev.* **2013**, *65*, 1299–1315.

[31] Pan, L. M.; He, Q. J.; Liu, J. N.; Chen, Y.; Ma, M.; Zhang, L. L.; Shi, J. L. Nuclear-targeted drug delivery of TAT peptide-conjugated monodisperse mesoporous silica nanoparticles. *J. Am. Chem. Soc.* **2012**, *134*, 5722–5725.

[32] Vivès, E.; Brodin, P.; Lebleu, B. A truncated HIV-1 TAT protein basic domain rapidly translocates through the plasma membrane and accumulates in the cell nucleus. *J. Biol. Chem.* **1997**, *272*, 16010–16017.

[33] Mattaj, I. W.; Englmeier, L. Nucleocytoplasmic transport: The soluble phase. *Annu. Rev. Biochem.* **1998**, *67*, 265–306.

[34] Torchilin, V. P. Tat peptide-mediated intracellular delivery of pharmaceutical nanocarriers. *Adv. Drug Deliv. Rev.* **2008**, *60*, 548–558.

[35] Hsu, P. P.; Sabatini, D. M. Cancer cell metabolism: Warburg and beyond. *Cell* **2008**, *134*, 703–707.

[36] Heiden, M. G. V.; Cantley, L. C.; Thompson, C. B. Understanding the warburg effect: The metabolic requirements of cell proliferation. *Science* **2009**, *324*, 1029–1033.

[37] Kelland, L. The resurgence of platinum-based cancer chemotherapy. *Nat. Rev. Cancer* **2007**, *7*, 573–584.

[38] Wheate, N. J.; Walker, S.; Craig, G. E.; Oun, R. The status of platinum anticancer drugs in the clinic and in clinical trials. *Dalton Trans.* **2010**, *39*, 8113–8127.

[39] Wang, X.; Yang, C. C.; Zhang, Y. J.; Zhen, X.; Wu, W.; Jiang, X. Q. Delivery of platinum(IV) drug to subcutaneous tumor and lung metastasis using bradykinin-potentiating peptide-decorated chitosan nanoparticles. *Biomaterials* **2014**, *35*, 6439–6453.

[40] Dhar, S.; Gu, F. X.; Langer, R.; Farokhzad, O. C.; Lippard, S. J. Targeted delivery of cisplatin to prostate cancer cells by aptamer functionalized Pt(IV) prodrug-plga-peg nanoparticles. *Proc. Natl. Acad. Sci. USA* **2008**, *105*, 17356–17361.

[41] Fu, L. Y.; Yuan, P.; Ruan, Z.; Liu, L.; Li, T. W.; Yan, L. F. Ultra-pH-sensitive polypeptide micelles with large fluorescence off/on ratio in near infrared range. *Polym. Chem.* **2017**, *8*, 1028–1038.

[42] Li, H. J.; Du, J. Z.; Du, X. J.; Xu, C. F.; Sun, C. Y.; Wang, H. X.; Cao, Z. T.; Yang, X. Z.; Zhu, Y. H.; Nie, S. M. et al. Stimuli-responsive clustered nanoparticles for improved tumor penetration and therapeutic efficacy. *Proc. Natl. Acad. Sci. USA* **2016**, *113*, 4164–4169.

[43] Mishra, A.; Lai, G. H.; Schmidt, N. W.; Sun, V. Z.; Rodriguez, A. R.; Tong, R.; Tang, L.; Cheng, J.; Deming, T. J.; Kamei, D. T. et al. Translocation of HIV TAT peptide and analogues induced by multiplexed membrane and cytoskeletal interactions. *Proc. Natl. Acad. Sci. USA* **2011**, *108*, 16883–16888.

[44] Xu, X. Y.; Xie, K.; Zhang, X. Q.; Pridgen, E. M.; Park, G. Y.; Cui, D. S.; Shi, J. J.; Wu, J.; Kantoff, P. W.; Lippard, S. J. et al. Enhancing tumor cell response to chemotherapy through nanoparticle-mediated codelivery of sirna and cisplatin prodrug. *Proc. Natl. Acad. Sci. USA* **2013**, *110*, 18638–18643.

[45] Han, K.; Zhang, J.; Zhang, W. Y.; Wang, S. B.; Xu, L. M.; Zhang, C.; Zhang, X. Z.; Han, H. Y. Tumor-triggered geometrical shape switch of chimeric peptide for enhanced *in vivo* tumor internalization and photodynamic therapy. *ACS Nano* **2017**, *11*, 3178–3188.

[46] Uhrich, K. E.; Cannizzaro, S. M.; Langer, R. S.; Shakesheff, K. M. Polymeric systems for controlled drug release. *Chem. Rev.* **1999**, *99*, 3181–3198.

[47] Markman, J. L.; Rekechenetskiy, A.; Holler, E.; Ljubimova, J. Y. Nanomedicine therapeutic approaches to overcome cancer drug resistance. *Adv. Drug Deliv. Rev.* **2013**, *65*, 1866–1879.

[48] Wu, M. Y.; Meng, Q. S.; Chen, Y.; Du, Y. Y.; Zhang, L. X.; Li, Y. P.; Zhang, L. L.; Shi, J. L. Large-pore ultrasmall mesoporous organosilica nanoparticles: Micelle/precursor co-templating assembly and nuclear-targeted gene delivery. *Adv. Mater.* **2015**, *27*, 215–222.

[49] Jin, E. L.; Zhang, B.; Sun, X. R.; Zhou, Z. X.; Ma, X. P.; Sun, Q. H.; Tang, J. B.; Shen, Y. Q.; Van Kirk, E.; Murdoch, W. J. et al. Acid-active cell-penetrating peptides for *in vivo* tumor-targeted drug delivery. *J. Am. Chem. Soc.* **2013**, *135*, 933–940.

[50] Sun, T. D.; Cui, W.; Yan, M.; Qin, G.; Guo, W.; Gu, H. X.; Liu, S. Q.; Wu, Q. Target delivery of a novel antitumor organoplatinum(IV)-substituted polyoxometalate complex for safer and more effective colorectal cancer therapy *in vivo*. *Adv. Mater.* **2016**, *28*, 7397–7404.

[51] Wang, X. Y.; Guo, Z. J. Targeting and delivery of platinum-based anticancer drugs. *Chem. Soc. Rev.* **2013**, *42*, 202–224.

[52] Petros, R. A.; DeSimone, J. M. Strategies in the design of nanoparticles for therapeutic applications. *Nat. Rev. Drug Discov.* **2010**, *9*, 615–627.

[53] Peer, D.; Karp, J. M.; Hong, S.; FaroKHzad, O. C.; Margalit, R.; Langer, R. Nanocarriers as an emerging platform for cancer therapy. *Nat. Nanotechnol.* **2007**, *2*, 751–760.

[54] Heldin, C. H.; Rubin, K.; Pietras, K.; Östman, A. High interstitial fluid pressure—An obstacle in cancer therapy. *Nat. Rev. Cancer* **2004**, *4*, 806–813.